
FATE: Pillar Encoding and Frequency-Aware Training for Event-Based Object Detection

Md Tawheedul Islam Bhuian Kyoung-Don Kang

School of Computing

State University of New York at Binghamton

{mislambhuian, kang}@binghamton.edu

Abstract

Event cameras are bio-inspired sensors that asynchronously capture logarithmic intensity changes, offering inherent advantages in high-speed and high-dynamic-range scenarios. However, the sparse and asynchronous nature of event streams poses a fundamental challenge for modern deep learning architectures. To enable compatibility with standard models, most existing approaches partition the accumulation window into fixed temporal sub-bins. While effective for spatial processing, this internal discretization discards fine-grained temporal structure and constrains inference to the low temporal frequencies imposed by training supervision. To address this limitation, we propose FATE, a unified framework built upon a novel Pillar Encoding (PE). While operating over discrete macro-accumulation windows dictated by the target frequency, PE avoids internal temporal sub-binning. It organizes events into spatial pillars and approximates their intra-window evolution via projection onto a continuous-time orthogonal polynomial basis. This formulation yields an L^2 -optimal representation that retains rich temporal dynamics in a dense pseudo-image, mitigating information loss under sparse event conditions. To fully leverage this representation, we introduce Frequency-Aware Training (FAT), a soft mean-teacher curriculum that generates temporally dense pseudo-labels, effectively bridging the mismatch between low-frequency supervision and high-frequency inference. Extensive experiments demonstrate that FATE generalizes across architectural paradigms and consistently outperforms strong baselines. It enables robust object detection at high temporal resolutions up to 200 Hz, while incurring minimal overhead in parameter count and inference latency.

1 Introduction

Event cameras introduce a fundamentally different paradigm for visual perception. Unlike conventional frame-based cameras that record absolute intensity at fixed intervals, event cameras operate asynchronously, emitting events only in response to local logarithmic brightness changes. This sensing mechanism provides fine-grained temporal resolution, high dynamic range, and minimal motion blur [13]. These properties make event cameras particularly well-suited for applications such as autonomous driving, robotics, and high-speed tracking, where conventional sensors often degrade under rapid motion or challenging lighting conditions.

Despite these advantages, effectively leveraging event data for downstream tasks such as object detection remains challenging. Modern architectures, including Convolutional Neural Networks (CNNs) and Vision Transformers (ViTs), assume dense, grid-structured inputs, rendering raw asynchronous event streams incompatible. Consequently, most approaches partition the macro-accumulation window into fixed temporal sub-bins or voxel grids to form dense representations [16, 37]. While this enables the use of standard backbones, it introduces a key limitation: internal temporal discretization.

Aggregating events via rigid sub-binning discards fine-grained temporal structure and implicitly constrains inference to low temporal frequencies present during training (e.g., 20 Hz), limiting performance at higher temporal resolutions.

To address this limitation, we propose **FATE**, a unified framework for high-frequency event-based object detection. At its core is **Pillar Encoding (PE)**. While PE operates over discrete macro-accumulation windows dictated by the target frequency, it avoids internal temporal sub-binning. By discretizing the spatial domain into pillars, PE models the within-pillar event evolution as a continuous-time signal. Specifically, asynchronous event features within each pillar are approximated via projection onto a truncated set of orthogonal Legendre polynomials, yielding a compact set of coefficients that encode temporal dynamics and mitigate information loss under sparse event conditions. This construction corresponds to an orthogonal projection onto a finite-dimensional subspace, yielding the minimizer of the L^2 reconstruction error under a fixed coefficient budget. As a result, PE preserves rich temporal structure while producing a dense pseudo-image compatible with standard architectures.

While PE enables continuous-time modeling, learning such representations introduces a second challenge: the scarcity of high-frequency annotations. Event-based datasets typically provide labels at low frame rates, creating a mismatch between training supervision and high-frequency inference. To bridge this gap, we propose **Frequency-Aware Training (FAT)**. FAT first generates temporally dense pseudo-labels via tracking-by-detection, and then applies a soft mean-teacher curriculum that progressively exposes the student model to higher-frequency inputs while enforcing consistency with low-frequency supervision.

Together, PE and FAT form a complementary framework that addresses both representation and supervision mismatches. We evaluate FATE on standard event-based object detection benchmarks and observe consistent improvements over strong baselines, with more pronounced gains in high-frequency regimes.

Contributions.

- **Pillar Encoding:** We introduce an event representation that avoids internal temporal sub-binning by modeling intra-window dynamics as continuous-time functions via orthogonal polynomial projections. Our formulation yields an L^2 -optimal approximation under truncation, efficiently preserving fine-grained temporal structure within the accumulation window.
- **Frequency-Aware Training:** We propose a training strategy that leverages temporally dense pseudo-labels and a mean-teacher curriculum to mitigate train–test frequency mismatch, enabling effective high-frequency inference without additional manual annotation.
- **Robust Empirical Performance:** FATE consistently outperforms strong baselines on major benchmarks, enabling robust object detection at temporal resolutions up to 200 Hz with minimal computational overhead, utilizing less than 0.15M additional parameters and a $\sim 1\%$ end-to-end inference latency increase.

2 Related Work

Event Representations. Event cameras output an asynchronous stream of events rather than synchronous intensity frames, yielding a signal that is spatially sparse and temporally irregular. Early approaches transformed these events into handcrafted, frame-like tensors for compatibility with standard vision architectures. Event histograms [40] and time surfaces [4, 24] aggregate events per pixel, discarding intermediate events prior to the most recent one. Stacked histograms [35] and voxel grids [52] partition timestamps into discrete temporal bins, while TORE volumes [3] retain the k most recent timestamps. Fundamentally, these representations rely on windowing or binning hyperparameters that trade temporal precision for stable tensor dimensions.

Alternatively, point-based methods preserve temporal fidelity by processing events as irregular point sets. EventNet [39] recursively updates global features, while graph-based methods [6, 11] apply message passing over spatiotemporal graphs. The asynchronous-to-synchronous (A2S) paradigm seeks a middle ground, encoding events asynchronously into a state that can be sampled by a synchronous backbone [21, 46]. However, recent findings [19] suggest that current A2S encoders still produce weaker representations relative to dense methods.

Learned grid representations, such as Matrix-LSTM [7] and differentiable event-to-grid frameworks [16], adapt the encoding to downstream tasks. However, these methods still operate on dense pixel grids and rely on pooling or recurrence, biasing representations toward high-density regions and limiting the preservation of continuous temporal dynamics.

Our work belongs to this family of learned representations but departs from dense temporal discretization. We draw inspiration from PointPillars [25, 29], which collapses irregular point clouds into spatial columns. While EventPillars [12] applies this idea to events using handcrafted statistics and primarily focuses on classification settings, we instead model temporal evolution for object detection in a learned manner. Building on orthogonal polynomial projections [41], we approximate event dynamics within each pillar as a continuous trajectory, producing a compact and expressive representation robust to sparse event distributions.

Event-Based Architectures. Driven by these representations, various architectures have been proposed for event-based object detection. Early CNN-based detectors [20, 35] applied standard networks to frame-like inputs, discarding the asynchronous nature of events. Subsequent works introduced explicit temporal modeling: RED [35] employs convolutional LSTMs, ASTMNet [28] leverages asynchronous spatio-temporal memory, and RVT [17] combines multi-scale transformers with recurrent processing for efficient detection at a fixed frequency (20 Hz). More recently, PLEIADES [32] proposes continuous-time temporal kernels parameterized via orthogonal polynomial bases.

Recent advances improve efficiency and temporal reasoning. These include group-wise event tokenization [33], scene-adaptive sparse attention [34], and state-space models [51, 53] for scalable long-range temporal modeling. Recent works such as EvRT-DETR [45] adapt pretrained image-based models to event data, while others explore spiking or hybrid ANN-SNN architectures for energy-efficient processing [2, 27, 43]. Additionally, multimodal transformer frameworks such as SODFormer [26] have emerged to fuse asynchronous event streams with complementary frame-based information.

Despite these advances, most architectures are trained and evaluated at a fixed, relatively low temporal frequency (e.g., 20 Hz), leading to degraded performance at higher frequencies with short accumulation windows [15]. To address related issues, FlexEvent [30] enables frequency adaptation via event-frame fusion but relies on synchronized RGB inputs. LEOD [49] improves supervision through self-training but does not explicitly address distribution shifts across multiple frequencies.

More recently, backbones focus on sparsity and high-frequency robustness. SMamba [51] leverages state-space modeling, SSLA-Det [18] introduces asynchronous linear attention for sparse processing, EMF [22] models per-pixel temporal dynamics via event progression, SEED [47] targets neuromorphic efficiency, and MvHeat-DET [48] employs heat-conduction mechanism to balance accuracy and efficiency. However, these methods primarily focus on backbone design and do not explicitly address pillar encoding or multi-frequency supervision. In contrast, FATE explicitly targets this gap by providing pillar encoding and supervision across multiple temporal resolutions without requiring paired RGB data or manual annotations of high-frequency events.

3 Method

3.1 Pillar Encoding

We transform raw event streams into an image-like representation. Prior methods (e.g., stacked 2D histograms [13]) rely on rigid temporal binning, which exacerbates sparsity in short windows. To address this, our PE discretizes space into pillars and models events within each pillar via a continuous-time polynomial approximation. The PE pipeline is illustrated in Figure 1 and described next.

Event Pillarization. Given a target inference frequency f , we define a macro-accumulation window $[t_1, t_2]$ of duration $\Delta t = 1/f$. The event stream within this window is denoted as a set of spatiotemporal points \mathcal{E} . To process these points, we first discretize the spatial domain into an evenly spaced grid in the $x - y$ plane, partitioning \mathcal{E} into a set of discrete spatial pillars \mathcal{P} indexed by $j \in \{1, \dots, P\}$. Crucially, we retain the continuous temporal precision of each event within its respective pillar. To ensure numerical stability and align with the canonical domain of the Legendre

polynomials, the absolute timestamp $t_i \in [t_1, t_2]$ of each event $e_i \in \mathcal{E}$ is normalized and centered as $\tau_i = 2 \left(\frac{t_i - t_1}{\Delta t} \right) - 1$, ensuring $\tau_i \in [-1, 1]$ and the center = 0.

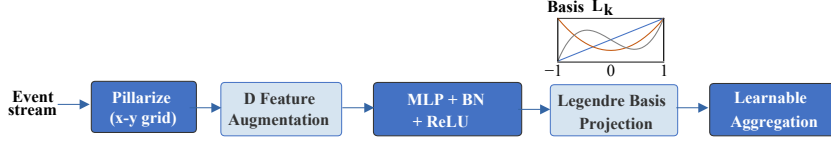


Figure 1: Pillar Encoding of FATE

Each event is augmented with local spatial and temporal offsets to provide a stronger inductive bias. Offsets from the pillar-wise event mean capture locally occupied centroids and temporal skew, while offsets from the pillar center define a consistent local coordinate. Together, these features encode both the spatial distribution and temporal layout of events within each pillar.

For the n -th event in pillar j , the resulting augmented representation is defined as a D dimensional feature vector:

$$l_{j,n} = (x_{j,n}, y_{j,n}, \tau_{j,n}, p_{j,n}, x_{j,n,m}, y_{j,n,m}, \tau_{j,n,m}, x_{j,n,c}, y_{j,n,c}), \quad (1)$$

where $(x_{j,n}, y_{j,n})$ denotes the location, $\tau_{j,n} \in [-1, 1]$ denotes the normalized timestamp of the n -th event in pillar j sorted in ascending timestamp order, and $p_{j,n}$ indicates the polarity (+1 or -1). The subscript m denotes the offset from the arithmetic mean of all events within the pillar. Moreover, let $(x_{j,c}, y_{j,c})$ denote the predefined center of the x -axis and y -axis of pillar j . Given that, $x_{j,n,c} = x_{j,n} - x_{j,c}$, $y_{j,n,c} = y_{j,n} - y_{j,c}$.

Due to the sparsity of event streams, the set of pillars is predominantly empty, and a non-empty pillar typically contains only a small number of events. We exploit this sparsity by capping the number of non-empty pillars per sample to P and the number of events per pillar to N , yielding a dense tensor representation of size (D, P, N) . If pillar j contains fewer than N events, it is zero-padded by appending dummy events to the end of its events already sorted in timestamp-order and assigning a mask value $m_{j,n} = 0$ to dummy event n in pillar j to avoid any processing.

Conversely, if a spatial pillar contains more than N events—a rare case under the high-frequency sparse regime we target—we apply uniform random subsampling, following [25]. We favor random subsampling over deterministic strategies to avoid temporal bias: truncation (e.g., retaining only the most recent events) would discard early temporal dynamics and distort the underlying event distribution. In contrast, random subsampling preserves the statistical properties of the event stream, enabling an effective approximation of the intra-window trajectory under our polynomial basis.

Event-Wise Feature Embedding. Following pillarization, we model each pillar as a *continuous-time signal*, rather than an unordered set of events or a stack of fixed temporal bins. This choice is motivated by the fact that different objects are characterized not only by the presence of events but also by the trajectory of how their features evolve over time within the pillar.

First, we assemble the augmented event vectors into a dense input tensor $\mathbf{X} \in \mathbb{R}^{D \times P \times N}$. For each event, a shared event-wise MLP, followed by BatchNorm and ReLU, maps the D -dimensional vector into a higher-dimensional latent space:

$$\mathbf{H} = \sigma(\text{BN}(\mathbf{W}\mathbf{X} + \mathbf{b})), \quad \mathbf{H} \in \mathbb{R}^{C \times P \times N} \quad (2)$$

where C is the latent feature dimension. Let $H_{c,j,n}$ denote the feature value of channel c for the n -th event in pillar j . We view each discrete feature $H_{c,j,n}$ as a point-sample of an underlying continuous function $h_{c,j}(\tau)$ that evolves over time within the pillar, such that $H_{c,j,n} \approx h_{c,j}(\tau_{j,n})$.

Continuous-Time Temporal Encoding via Polynomial Approximation. To rigorously model these within-pillar dynamics, we project the latent feature trajectory $h_{c,j}(\tau)$ onto a set of orthogonal polynomial basis functions defined over the Hilbert space $\mathcal{H} = L^2([-1, 1])$. We select the Legendre polynomials [1], denoted as $L_k(\tau)$ for degree $k \in \{0, \dots, K-1\}$, because they form a complete orthogonal basis on $[-1, 1]$ satisfying:

$$\langle L_k, L_m \rangle = \int_{-1}^1 L_k(\tau) L_m(\tau) d\tau = \frac{2}{2k+1} \delta_{km}, \quad (3)$$

where δ_{km} is the Kronecker delta. By the Hilbert projection theorem [23, 31], any square-integrable temporal signal can be exactly expanded as an infinite series $h_{c,j}(\tau) = \sum_{k=0}^{\infty} a_{c,j,k} L_k(\tau)$. The exact

projection coefficients $a_{c,j,k}$ are obtained via the inner product:

$$a_{c,j,k} = \frac{2k+1}{2} \int_{-1}^1 h_{c,j}(\tau) L_k(\tau) d\tau. \quad (4)$$

In practice, to maintain a computationally tractable, fixed-size representation for the neural network, we restrict our model to a K -dimensional subspace by computing a truncated Legendre expansion up to degree $K - 1$. Crucially, the Hilbert projection theorem guarantees that this specific orthogonal projection yields the optimal approximation of the true continuous signal $h_{c,j}(\tau)$ within this subspace, minimizing the L^2 reconstruction error. A common practice is to select a value of K value that supports reliable performance at minimal overhead, beyond which improvement is marginal. Physically, in this optimal truncated representation, lower-order terms (e.g., $k = 0, 1$) capture coarse temporal trends such as constant presence or linear drift, while higher-order terms encode fine-grained, non-linear variations in the event features without introducing arbitrary temporal binning.

In practice, the analytic function $h_{c,j}(\tau)$ is unobservable; we only have access to irregular, sparse samples $\{H_{c,j,n}\}$ at discrete timestamps $\{\tau_{j,n}\}$. Therefore, the continuous integral must be approximated numerically. Because event timestamps are generally non-uniformly distributed, naive mean or max pooling produces a highly biased estimate. To obtain a consistent, unbiased estimate, we approximate the temporal integral using numerical quadrature adapted for non-uniform temporal grids. Specifically, we utilize the trapezoidal rule [9, 36], which assigns a temporal support weight $w_{j,n}$ to each event based on its local sparsity:

$$w_{j,n} = \begin{cases} \frac{1}{2}(\tau_{j,2} - \tau_{j,1}), & n = 1, \\ \frac{1}{2}(\tau_{j,n+1} - \tau_{j,n-1}), & 1 < n < N, \\ \frac{1}{2}(\tau_{j,N} - \tau_{j,N-1}), & n = N. \end{cases} \quad (5)$$

Under this formulation, isolated events correctly represent larger temporal chunks, while tightly clustered events receive smaller individual weights, preventing rapid event bursts from disproportionately dominating the integral.

Using these weights, we compute the quadrature-corrected empirical moments $z_{c,j,k}$, which estimate the projection of the discrete event features onto the k -th Legendre polynomial:

$$z_{c,j,k} = \frac{1}{W_j} \sum_{n=1}^N m_{j,n} w_{j,n} H_{c,j,n} L_k(\tau_{j,n}) \quad W_j = \sum_{n=1}^N m_{j,n} w_{j,n} \quad (6)$$

where $m_{j,n} \in \{0, 1\}$ acts as a validity mask for zero-padded events in pillars with fewer than N entries. Note that the constant Legendre scaling factor $\frac{2k+1}{2}$ from the exact analytical projection is omitted in this estimator, as it is naturally absorbed by the learnable linear coefficients in the subsequent layer. The normalization by W_j ensures that the encoded features remain invariant to the total temporal active duration of the pillar.

Learnable Aggregation. Finally, we linearly combine the K temporal moments using learnable per-channel coefficients to form the final pillar representation:

$$r_{c,j} = \sum_{k=0}^{K-1} \alpha_{c,k} z_{c,j,k} + \beta_c \quad \mathbf{R} \in \mathbb{R}^{C \times P} \quad (7)$$

where $\alpha \in \mathbb{R}^{C \times K}$ and $\beta \in \mathbb{R}^C$ are trainable parameters. These coefficients introduce only $C(K + 1)$ additional parameters, making the encoding highly efficient. The parameters C and K act as tunable hyperparameters.

Once encoded, the features are scattered back to their original spatial locations to create a pseudo-image of size (C, H, W) . This pillar-based continuous-time representation enables efficient spatial feature learning while retaining the rich, asynchronous temporal dynamics of the raw event stream. At high inference frequencies (e.g., 200 Hz), Δt is sufficiently small that cross-pillar motion blur is minimized; residual spatial trajectories are effectively aggregated by the receptive field of the downstream backbone.

Our PE formulation is grounded in two theoretical guarantees (proofs provided in Appendix A). First, by defining the coefficients as in Eq. 4, our truncated Legendre series acts as the unique

Algorithm 1 Pillar Encoding (PE)

Input: Raw event set E from temporal window $[t_1, t_2]$, spatial grid size $H \times W$
Parameters: Max pillars P , max events N , polynomial degrees K , latent dims C
Output: Dense pseudo-image tensor $\mathbf{I} \in \mathbb{R}^{C \times H \times W}$

- 1: Discretize E into spatial pillars. Retain up to P non-empty pillars.
- 2: **for** each pillar $j \in \{1, \dots, P\}$ **do**
- 3: Subsample events, or zero-pad events and append them to exactly N .
- 4: Set $m_{j,n} = 0$ if event n is zero padded; otherwise, $m_{j,n} = 1$ (real event).
- 5: Normalize absolute timestamps to $\tau_{j,n} \in [-1, 1]$.
- 6: Sort intra-pillar events such that $\tau_{j,1} \leq \tau_{j,2} \dots \leq \tau_{j,N}$ for each event n with $m_{j,n} = 1$.
- 7: Compute temporal and spatial offsets (mean-centered and spatial/temporal-centered).
- 8: Construct the D -dimensional augmented feature vectors $l_{j,n}$.
- 9: Compute non-uniform trapezoidal weights $w_{j,n}$ based on local sparsity (Eq. 5).
- 10: Compute pillar weight normalizer: $W_j \leftarrow \sum_{n=1}^N m_{j,n} w_{j,n}$
- 11: **end for**
- 12: Assemble tensor $\mathbf{X} \in \mathbb{R}^{D \times P \times N}$ from $\{l_{j,n}\}$.
- 13: Extract latent features via shared MLP: $\mathbf{H} \leftarrow \sigma(\text{BN}(\mathbf{W}\mathbf{X} + \mathbf{b}))$
- 14: **for** each pillar $j \in \{1, \dots, P\}$ and channel $c \in \{1, \dots, C\}$ **do**
- 15: **for** degree $k \in \{0, \dots, K-1\}$ **do**
- 16: Compute quadrature-corrected empirical moment (Eq. 6):
- 17: $z_{c,j,k} \leftarrow \frac{1}{W_j} \sum_{n=1}^N m_{j,n} w_{j,n} H_{c,j,n} L_k(\tau_{j,n})$
- 18: **end for**
- 19: Linearly combine temporal moments using learnable weights (Eq. 7):
- 20: $r_{c,j} \leftarrow \sum_{k=0}^{K-1} \alpha_{c,k} z_{c,j,k} + \beta_c$
- 21: **end for**
- 22: Scatter pillar representations $\mathbf{R} \in \mathbb{R}^{C \times P}$ back to the $H \times W$ spatial grid to form \mathbf{I} .
- 23: **return** \mathbf{I}

orthogonal projection of the underlying signal $h_{c,j}(\tau)$ for all c, j at τ onto the subspace of Legendre polynomials, minimizing the L^2 reconstruction error. Second, our quadrature estimator in Eqs. 5 and 6 asymptotically recovers the true projection integral. Our pseudocode is detailed in Algorithm 1.

3.2 Frequency-Aware Training

We divide our training strategy into two sequential phases. First, we obtain dense supervision at multiple temporal frequencies. Second, we utilize a soft mean-teacher curriculum to enforce representational robustness across these frequencies.

Phase 1: Multi-Frequency Bounding Box Generation. The first phase aims to construct dense, frequency-specific annotations from sparsely labeled data. Let \mathcal{E} denote the event stream, and $\{(t_k, \mathcal{B}_{t_k})\}$ the sparse ground-truth annotations available only at canonical timestamps t_k , which typically correspond to a canonical frequency f_c (e.g., 20 Hz). Because annotations are not available at higher temporal frequencies, we first train an event detector, e.g., EvRT-DETR [45], augmented by the proposed PE using the original labeled data in the canonical setting.

Based on this PE-augmented detector, we generate dense annotations at target frequencies $f \in \mathcal{F} = \{f_{\min}, \dots, f_{\max}\}$ by running inference at interpolated timestamps in a sliding-window manner. For a target frequency f , the detector is applied at uniformly spaced inference timestamps $t_k = k \cdot \Delta t_f$, where $\Delta t_f = 1/f$. Each input is constructed using a fixed canonical accumulation window $\Delta t_c = 1/f_c$ over the interval $[t_k - \Delta t_c, t_k]$, effectively decoupling the temporal sampling rate from the event representation. We generate annotations progressively (e.g., first at 40 Hz, scaling up to 200 Hz), consistently maintaining temporal association through tracking-by-detection [5].

To ensure high-quality supervision, we adopt decoupled thresholds: a lower tracking threshold (e.g., 0.3) to favor recall by reducing missed detections, and a higher detection threshold (e.g., 0.6) to promote precision by limiting false positives (see Appendices B and D for details). We then associate detections across time and discard short tracklets as spurious. To account for denser sampling at

higher frequencies, the minimum tracklet length is increased proportionally with f . The remaining reliable trajectories are used to interpolate annotations at timestamps with missing detections.

The resulting dense, frequency-specific training set is $\tilde{\mathcal{D}}_f = \{(\mathbf{r}_{f,i}, \tilde{\mathcal{B}}_{f,i})\}_{i=1}^{M_f}$, where $\mathbf{r}_{f,i}$ denotes an event representation—PE output—at frequency f , and $\tilde{\mathcal{B}}_{f,i}$ the corresponding supervision, consisting of either ground-truth annotations or labels interpolated along tracked trajectories. Notably, these dense pseudo labels (bounding boxes) are used to enable offline FAT, but are not utilized during online inference in FATE.

Phase 2: Soft Mean-Teacher Self-Training. The proposed frequency-aware self-training adopts a soft mean-teacher framework [44, 50]. In particular, it exploits three sources of supervision: (i) ground-truth annotations at the originally labeled timestamps, (ii) interpolated labels from Phase 1, and (iii) pseudo-labels produced by the teacher network during self-training. The first two provide explicit supervision, while the third provides a teacher–student consistency constraint that regularizes the student model.

Let \mathbf{R}_f and \mathbf{R}_c denote the sets of event representations at frequencies f and f_c (canonical frequency). We write $\mathbf{r}_f \in \mathbf{R}_f$ and $\mathbf{r}_c \in \mathbf{R}_c$ for individual samples. The teacher network processes \mathbf{r}_c , while the student network processes \mathbf{r}_f . Given inputs \mathbf{r}_f and \mathbf{r}_c , a student network S_{θ_s} and a teacher network T_{θ_t} output predictions:

$$\{(s_{s,j}, b_{s,j})\}_{j=1}^{N_s} = S_{\theta_s}(\mathbf{r}_f), \quad \{(s_{t,j}, b_{t,j})\}_{j=1}^{N_t} = T_{\theta_t}(\mathbf{r}_c). \quad (8)$$

Instead of uniformly sampling frequencies, we employ a linear curriculum schedule over the frequency-specific datasets. At training round r , the student frequency is sampled according to $f \sim p_r(f)$, which gradually shifts the probability mass toward higher, sparser frequencies as training progresses.

For bounding box regression, the DETR [8] head uses a weighted combination of ℓ_1 and GIoU losses, while the YOLOX [14] head primarily uses the standard IoU regression loss:

$$\mathcal{L}_{\text{box}}(b, \hat{b}) = \lambda_{\ell_1} \|b - \hat{b}\|_1 + \lambda_{\text{iou}} \mathcal{L}_{\text{GIoU}}(b, \hat{b}) \quad (9)$$

For the DETR head, let \mathcal{M}_i denote the set of matched prediction–target pairs for sample i , established via bipartite matching. While the regression loss \mathcal{L}_{box} is evaluated exclusively over this matched set \mathcal{M}_i , the classification loss explicitly penalizes all remaining mismatched predictions as a "no object" (\emptyset) background class, a mechanism crucial for suppressing false positive detections.

Each target is represented as a pair (c_v, b_v) , where c_v denotes the class label and $b_v \in \mathbb{R}^4$ the corresponding ground-truth bounding box. Given that, the detection objective is formulated as:

$$\mathcal{L}_{\text{det}} = \frac{1}{|\mathcal{U}|} \sum_{i \in \mathcal{U}} \left[\sum_{(u,v) \in \mathcal{M}_i} w_v (\ell_{\text{cls}}(s_{s,u}, c_v) + \ell_{\text{box}}(b_{s,u}, b_v)) + \sum_{u \notin \mathcal{M}_i} \ell_{\text{cls}}(s_{s,u}, \emptyset) \right] \quad (10)$$

where \mathcal{U} is the mini-batch. The supervision weight w_v distinguishes ground-truth labels from generated labels:

$$w_v = \begin{cases} 1, & \text{if } (c_v, b_v) \text{ is a ground-truth annotation;} \\ p_v, & \text{if } (c_v, b_v) \text{ is a label generated in Phase 1,} \end{cases} \quad (11)$$

where $p_v \in [0, 1]$ denotes the scalar confidence assigned by the teacher to the matched generated label.

Additionally, we impose a consistency loss between the teacher’s canonical predictions and the student’s high-frequency predictions. The teacher network provides pseudo-labels during training, which serve as soft targets for regularizing the student model. We use Kullback–Leibler (KL) divergence for classification consistency and ℓ_1 loss for localization consistency:

$$\mathcal{L}_{\text{cons}} = \frac{1}{|\mathcal{U}|} \sum_{i \in \mathcal{U}} \frac{1}{|\mathcal{A}_i|} \sum_{(u,v) \in \mathcal{A}_i} [\text{KL}(q_{t,v} \| q_{s,u}) + \|b_{t,v} - b_{s,u}\|_1], \quad (12)$$

where \mathcal{A}_i denotes the set of matched teacher–student prediction pairs for sample i obtained via Hungarian matching [8]. Moreover, $q_{t,v}$ and $q_{s,u}$ (respectively, $b_{t,v}$ and $b_{s,u}$) denote the class

probability distributions over K object categories (bounding box predictions) produced by the teacher and student networks.

The student weights θ_s are updated via gradient descent, while the teacher weights θ_t are updated using an exponential moving average (EMA):

$$\theta_t \leftarrow \gamma\theta_t + (1 - \gamma)\theta_s, \quad \gamma \in [0, 1]. \quad (13)$$

Rather than strictly inheriting canonical-frequency blind spots, our temporal tracking interpolation actively recovers missing intermediate detections, while the EMA-based curriculum mitigates the risk of the student overfitting to isolated base-detector errors.

4 Evaluation

We evaluate FATE against recent event-based object detection methods on two standard benchmarks, analyzing performance across a range of temporal frequencies.

4.1 Evaluation Setup

Datasets. Experiments are conducted on Gen1 [10] and 1Mpx [35], which differ substantially in spatial resolution and event density. This setup enables evaluation under both sparse and high-resolution regimes, assessing robustness and scalability. Gen1 provides sparse annotations from first-generation sensors (1–4,Hz), whereas 1Mpx leverages fourth-generation sensors with significantly higher temporal density (~ 60 Hz). To study frequency generalization, we evaluate models at the canonical 50 ms window (20 Hz), as well as under shorter temporal windows corresponding to higher frequencies from 40 Hz to 200 Hz (25–5 ms).

Baselines and Implementation Details. We compare FATE against four state-of-the-art baselines: RVT-B [17], GET [33], S5-ViT-B [53], and EvRT-DETR-B [45], spanning convolutional, recurrent, transformer, and state-space paradigms. To evaluate mAP, we integrate FATE into two representative detectors: S5-ViT-B (S5-ViT backbone, YOLOX head) and EvRT-DETR (ResNet-50 backbone, recurrent transformer). Baselines use official checkpoints for fairness. See Appendix D for full implementation details.

4.2 Comparison to State-of-the-Art

Table 1: mAP at different operating frequencies on the Gen1 test set

Model	Frequency (Hz)				
	20 Hz	40 Hz	80 Hz	100 Hz	200 Hz
RVT-B [17]	47.20	35.13	21.98	18.61	8.35
GET [33]	47.90	34.15	19.97	15.13	5.35
S5-ViT-B [53]	47.40	46.44	45.08	42.49	39.84
EvRT-DETR-B [45]	<u>52.70</u>	<u>50.60</u>	45.00	42.20	32.00
FATE-S (PE + FAT + S5-ViT-B)	48.20	46.90	<u>47.02</u>	<u>43.18</u>	<u>40.80</u>
FATE-E (PE + FAT + EvRT-DETR-B)	53.14	51.60	48.40	46.80	42.38

Table 2: mAP at different operating frequencies on the 1Mpx test set

Model	Frequency (Hz)				
	20 Hz	40 Hz	80 Hz	100 Hz	200 Hz
RVT-B [17]	47.40	42.51	33.20	30.29	16.36
GET [33]	48.40	40.51	30.30	28.11	15.44
S5-ViT-B [53]	47.20	46.49	46.11	45.80	39.70
EvRT-DETR-B [45]	<u>50.40</u>	48.20	43.10	41.00	33.40
FATE-S (PE + FAT + S5-ViT-B)	48.80	<u>48.26</u>	47.30	46.14	<u>40.20</u>
FATE-E (PE + FAT + EvRT-DETR-B)	51.04	48.90	<u>46.32</u>	<u>45.77</u>	40.54

As frequency increases, all methods degrade due to extreme sparsity from shorter accumulation windows (Tables 1 and 2). However, FATE consistently outperforms prior work, with gains that become more pronounced at higher frequencies. At 20 Hz, **FATE-E** achieves 53.14 mAP on Gen1 and 51.04 mAP on 1Mpx, improving over EvRT-DETR-B by +0.44 and +0.64 mAP. Under the most challenging 200 Hz setting, the margin widens substantially: FATE-E exceeds the strongest

high-frequency baseline (S5-ViT-B) by +2.54 mAP on Gen1 and +0.84 mAP on 1Mpx, demonstrating strong robustness under extreme sparsity.

Importantly, these gains generalize across different architectural paradigms. Integrating FATE into S5-ViT-B (FATE-S) also yields consistent improvements over S5-ViT-B, particularly in high-frequency regimes (+0.96 mAP on Gen1 and +0.50 mAP on 1Mpx at 200 Hz). This confirms that FATE’s benefits are not tied to a specific detector design, but rather address fundamental challenges in event-based representation and supervision-inference frequency mismatch.

Qualitative results (Appendix C) show that under short temporal windows, FATE maintains stable predictions—especially for small or weak targets—avoiding the missed detections of competing methods. These gains incur negligible overhead (+0.1 ms latency, less than 0.15 M parameters; Appendix B). This robustness stems from: (i) continuous-time polynomial pillar encoding, which preserves fine-grained temporal dynamics under sparsity, and (ii) frequency-aware training, which mitigates train–test mismatch across temporal resolutions.

4.3 Ablation Study

Tables 3 and 4 ablate PE and FAT on Gen1, confirming both are critical for sparse, high-frequency inference. PE outperforms baselines in 6/10 settings (e.g., +4.40 mAP at 200 Hz over EvRT-DETR-B) by preserving intra-window temporal dynamics. FAT yields even broader gains, leading in 9/10 settings (e.g., +9.10 mAP at 200,Hz over EvRT-DETR-B), proving that multi-frequency supervision mitigates train–test mismatch without adding capacity overhead.

Combined, PE and FAT achieve the best overall performance, supporting our central claim that robust temporal scaling requires both continuous representations and frequency-aligned supervision. Additional ablations on frequency-aware training strategies, polynomial degree K , pillar size, and temporal capacity C are provided in Appendix B.

Summary. PE alleviates the representational bottleneck of short event windows, FAT mitigates cross-frequency supervision mismatch, and their combination enables strong performance across frequencies.

Table 3: Ablation of the FATE-E (PE + FAT + EvRT-DETR-B) components on the Gen1 test set

Setting	mAP (%) \uparrow					Model Size
	20 Hz	40 Hz	80 Hz	100 Hz	200 Hz	#Params (M)
EvRT-DETR-B	52.70	50.60	45.00	42.20	32.00	57.14
+ PE	51.94	50.31	46.06	44.10	36.40	57.16
+ FAT	<u>52.36</u>	<u>51.24</u>	48.50	46.48	<u>41.10</u>	57.14
+ PE + FAT	53.14	51.60	<u>48.40</u>	46.80	42.38	57.16

Table 4: Ablation of the FATE-S (PE + FAT + S5-ViT-B) components on the Gen1 test set

Setting	mAP (%) \uparrow					Model Size
	20 Hz	40 Hz	80 Hz	100 Hz	200 Hz	#Params (M)
S5-ViT-B	47.40	46.44	45.08	42.49	39.84	18.19
+ PE	47.70	46.10	45.52	43.08	39.30	18.33
+ FAT	<u>48.08</u>	<u>46.78</u>	<u>46.50</u>	43.24	<u>40.38</u>	18.19
+ PE + FAT	48.20	46.90	47.02	<u>43.18</u>	40.80	18.33

5 Conclusion

To alleviate a fundamental limitation in event-based object detection—performance degradation at high operating frequencies due to event sparsity—we introduced the FATE framework, uniting Pillar Encoding (PE) with Frequency-Aware Training (FAT). PE provides a continuous-time, L^2 -optimal polynomial representation that retains fine-grained temporal dynamics while avoiding internal temporal sub-binning. Concurrently, FAT mitigates the train–test frequency mismatch by leveraging temporally dense pseudo-labels to promote robustness across the frequency spectrum. By generalizing across different architectural paradigms, FATE consistently outperforms strong baselines, with higher performance gains under high-frequency conditions (up to 200 Hz). Overall, our results underscore the critical importance of continuous-time modeling and cross-frequency supervision for robust, high-speed event-based perception.

References

- [1] Milton Abramowitz and Irene A Stegun. *Handbook of Mathematical Functions with Formulas, Graphs, and Mathematical Tables*, volume 55. US Department of Commerce, National Bureau of Standards, Washington, D.C., 1964.
- [2] Asude Aydin, Mathias Gehrig, Daniel Gehrig, and Davide Scaramuzza. A hybrid ANN-SNN architecture for low-power and low-latency visual perception. In *Proceedings of the IEEE/CVF Conference on Computer Vision and Pattern Recognition (CVPR) Workshops*, 2024.
- [3] R. Wes Baldwin, Ruixu Liu, Mohammed Almatrafi, Vijayan Asari, and Keigo Hirakawa. Time-Ordered Recent Event (TORE) Volumes for Event Cameras. *IEEE Transactions on Pattern Analysis and Machine Intelligence*, 45(2):2519–2532, 2023. ISSN 1939-3539. doi: 10.1109/TPAMI.2022.3172212.
- [4] Ryad Benosman, Charles Clercq, Xavier Lagorce, Sio-Hoi Ieng, and Chiara Bartolozzi. Event-based visual flow. *IEEE Transactions on Neural Networks and Learning Systems*, 25(2): 407–417, 2013. doi: 10.1109/TNNLS.2013.2273537.
- [5] Alex Bewley, Zongyuan Ge, Lionel Ott, Fabio Ramos, and Ben Uppcroft. Simple online and realtime tracking. In *2016 IEEE International Conference on Image Processing (ICIP)*, pages 3464–3468, Phoenix, AZ, USA, September 2016. IEEE. doi: 10.1109/ICIP.2016.7533003.
- [6] Yin Bi, Aaron Chadha, Alhabib Abbas, Eirina Bourtsoulatze, and Yiannis Andreopoulos. Graph-Based Spatio-Temporal Feature Learning for Neuromorphic Vision Sensing. *IEEE Transactions on Image Processing*, 29:9084–9098, 2020. ISSN 1941-0042. doi: 10.1109/TIP.2020.3023597.
- [7] Marco Cannici, Marco Ciccone, Andrea Romanoni, and Matteo Matteucci. A differentiable recurrent surface for asynchronous event-based data. In *The European Conference on Computer Vision (ECCV)*, August 2020.
- [8] Nicolas Carion, Francisco Massa, Gabriel Synnaeve, Nicolas Usunier, Alexander Kirillov, and Sergey Zagoruyko. End-to-End Object Detection with Transformers. In Andrea Vedaldi, Horst Bischof, Thomas Brox, and Jan-Michael Frahm, editors, *Computer Vision – ECCV 2020*, volume 12346, pages 213–229. Springer International Publishing. doi: 10.1007/978-3-030-58452-8_13.
- [9] Philip J Davis and Philip Rabinowitz. *Methods of Numerical Integration*. Courier Corporation, 2007.
- [10] Pierre de Tournemire, Davide Nitti, Etienne Perot, Davide Migliore, and Amos Sironi. A Large Scale Event-based Detection Dataset for Automotive, 2020.
- [11] Yongjian Deng, Hao Chen, Hai Liu, and Youfu Li. A Voxel Graph CNN for Object Classification with Event Cameras. In *2022 IEEE/CVF Conference on Computer Vision and Pattern Recognition (CVPR)*, pages 1162–1171, 2022. doi: 10.1109/CVPR52688.2022.00124.
- [12] Rui Fan, Weidong Hao, Juntao Guan, Lai Rui, Lin Gu, Tong Wu, Fanhong Zeng, and Zhangming Zhu. Eventpillars: Pillar-based efficient representations for event data. *Proceedings of the AAAI Conference on Artificial Intelligence*, 39(3):2861–2869, 2025. doi: 10.1609/aaai.v39i3.32292.
- [13] Guillermo Gallego, Tobi Delbrück, Garrick Orchard, Chiara Bartolozzi, Brian Taba, Andrea Censi, Stefan Leutenegger, Andrew J. Davison, Jörg Conradt, Kostas Daniilidis, et al. Event-based vision: A survey. *IEEE Transactions on Pattern Analysis and Machine Intelligence*, 44(1):154–180, 2020.
- [14] Zheng Ge, Songtao Liu, Feng Wang, Zeming Li, and Jian Sun. Yolox: Exceeding yolo series in 2021. *arXiv preprint arXiv:2107.08430*, 2021.
- [15] Daniel Gehrig and Davide Scaramuzza. Low-latency automotive vision with event cameras. *Nature*, 629(8014):1034–1040. ISSN 0028-0836, 1476-4687. doi: 10.1038/s41586-024-07409-w.
- [16] Daniel Gehrig, Antonio Loquercio, Konstantinos G. Derpanis, and Davide Scaramuzza. End-to-end learning of representations for asynchronous event-based data. In *Proceedings of the IEEE/CVF International Conference on Computer Vision (ICCV)*, pages 5633–5643, 2019.

- [17] Mathias Gehrig and Davide Scaramuzza. Recurrent Vision Transformers for Object Detection with Event Cameras. In *2023 IEEE/CVF Conference on Computer Vision and Pattern Recognition (CVPR)*, pages 13884–13893, 2023. doi: 10.1109/CVPR52729.2023.01334.
- [18] Haiqing Hao, Zhipeng Sui, Rong Zou, Zijia Dai, Nikola Zubić, Davide Scaramuzza, and Wenhui Wang. Low-latency event-based object detection with spatially-sparse linear attention. *arXiv preprint arXiv:2603.06228*, 2026.
- [19] Haiqing Hao, Nikola Zubic, Weihua He, Zhipeng Sui, Davide Scaramuzza, and Wenhui Wang. Maximizing asynchronicity in event-based neural networks. In *The Fourteenth International Conference on Learning Representations*, 2026.
- [20] Zhuangyi Jiang, Pengfei Xia, Kai Huang, Walter Stechele, Guang Chen, Zhenshan Bing, and Alois Knoll. Mixed Frame-/Event-Driven Fast Pedestrian Detection. In *2019 International Conference on Robotics and Automation (ICRA)*, pages 8332–8338, 2019. doi: 10.1109/ICRA.2019.8793924.
- [21] Uday Kamal, Saurabh Dash, and Saibal Mukhopadhyay. Associative Memory Augmented Asynchronous Spatiotemporal Representation Learning for Event-based Perception. In *International Conference on Learning Representations (ICLR)*, 2023.
- [22] Muhammad Ahmed Ullah Khan, Abdul Hannan Khan, and Andreas Dengel. Emf: Event metaformers for event-based real-time traffic object detection. *arXiv preprint arXiv:2504.04124*, 2025.
- [23] Erwin Kreyszig. *Introductory Functional Analysis with Applications*, volume 1. John Wiley & Sons, New York, 1978.
- [24] Xavier Lagorce, Garrick Orchard, Francesco Galluppi, Bertram E. Shi, and Ryad B. Benosman. HOTS: A Hierarchy of Event-Based Time-Surfaces for Pattern Recognition. 39(7):1346–1359, 2017. ISSN 1939-3539. doi: 10.1109/TPAML.2016.2574707.
- [25] Alex H. Lang, Sourabh Vora, Holger Caesar, Lubing Zhou, Jiong Yang, and Oscar Beijbom. PointPillars: Fast Encoders for Object Detection From Point Clouds. In *2019 IEEE/CVF Conference on Computer Vision and Pattern Recognition (CVPR)*, pages 12689–12697, Long Beach, CA, USA, June 2019. IEEE. doi: 10.1109/CVPR.2019.01298.
- [26] Dianze Li, Jianing Li, and Yonghong Tian. SODFormer: Streaming object detection with transformer using events and frames. *arXiv preprint arXiv:2308.04047*, 2023.
- [27] Dianze Li, Jianing Li, Xu Liu, Zhaokun Zhou, Xiaopeng Fan, and Yonghong Tian. HDI-Former: Hybrid dynamic interaction ANN-SNN transformer for object detection using frames and events. *arXiv preprint arXiv:2411.18658*, 2024.
- [28] Jianing Li, Jia Li, Lin Zhu, Xijie Xiang, Tiejun Huang, and Yonghong Tian. Asynchronous spatio-temporal memory network for continuous event-based object detection. *IEEE Transactions on Image Processing*, 31:2975–2987, 2022. doi: 10.1109/TIP.2022.3162962.
- [29] Yishi Li, Yuhao Zhang, and Rui Lai. TinypillarNet: Tiny pillar-based network for 3d point cloud object detection at edge. *IEEE Transactions on Circuits and Systems for Video Technology*, 34(3):1772–1785, 2024. doi: 10.1109/TCSVT.2023.3297620.
- [30] Dongyue Lu, Lingdong Kong, Gim Hee Lee, Camille Simon Chane, and Wei Tsang Ooi. Flexevent: Towards flexible event-frame object detection at varying operational frequencies. In *The Thirty-ninth Annual Conference on Neural Information Processing Systems*, 2026.
- [31] David G Luenberger. *Optimization by Vector Space Methods*. John Wiley & Sons, New York, 1997.
- [32] Yan Ru Pei and Olivier JMD Coenen. PLEIADES: Building temporal kernels with orthogonal polynomials. In *The Thirty-ninth Annual Conference on Neural Information Processing Systems*, 2026.

- [33] Yansong Peng, Yueyi Zhang, Zhiwei Xiong, Xiaoyan Sun, and Feng Wu. GET: Group Event Transformer for Event-Based Vision. In *2023 IEEE/CVF International Conference on Computer Vision (ICCV)*, pages 6015–6025, 2023. doi: 10.1109/ICCV51070.2023.00555.
- [34] Yansong Peng, Hebei Li, Yueyi Zhang, Xiaoyan Sun, and Feng Wu. Scene Adaptive Sparse Transformer for Event-based Object Detection. In *2024 IEEE/CVF Conference on Computer Vision and Pattern Recognition (CVPR)*, pages 16794–16804, 2024. doi: 10.1109/CVPR52733.2024.01589.
- [35] Etienne Perot, Pierre de Tournemire, Davide Nitti, Jonathan Masci, and Amos Sironi. Learning to detect objects with a 1 megapixel event camera. In H. Larochelle, M. Ranzato, R. Hadsell, M.F. Balcan, and H. Lin, editors, *Advances in Neural Information Processing Systems*, volume 33, pages 16639–16652. Curran Associates, Inc., 2020.
- [36] William H Press, Saul A Teukolsky, William T Vetterling, and Brian P Flannery. *Numerical Recipes 3rd Edition: The Art of Scientific Computing*. Cambridge University Press, Cambridge, UK, 2007.
- [37] Henri Rebecq, René Ranftl, Vladlen Koltun, and Davide Scaramuzza. Events-to-video: Bringing modern computer vision to event cameras. In *Proceedings of the IEEE/CVF Conference on Computer Vision and Pattern Recognition (CVPR)*, pages 3857–3866, 2019.
- [38] Walter Rudin. *Principles of Mathematical Analysis*. McGraw-Hill, New York, 3rd edition, 1976.
- [39] Yusuke Sekikawa, Kosuke Hara, and Hideo Saito. EventNet: Asynchronous Recursive Event Processing. In *2019 IEEE/CVF Conference on Computer Vision and Pattern Recognition (CVPR)*, pages 3882–3891. IEEE. doi: 10.1109/CVPR.2019.00401.
- [40] Amos Sironi, Manuele Brambilla, Nicolas Bourdis, Xavier Lagorce, and Ryad Benosman. HATS: Histograms of Averaged Time Surfaces for Robust Event-Based Object Classification. In *2018 IEEE/CVF Conference on Computer Vision and Pattern Recognition*, pages 1731–1740, 2018. doi: 10.1109/CVPR.2018.00186.
- [41] Jimmy T.H. Smith, Andrew Warrington, and Scott Linderman. Simplified state space layers for sequence modeling. In *The Eleventh International Conference on Learning Representations*, 2023.
- [42] Leslie N Smith and Nicholay Topin. Super-convergence: very fast training of neural networks using large learning rates. In *Artificial Intelligence and Machine Learning for Multi-Domain Operations Applications*, volume 11006, page 1100612. SPIE, 2019.
- [43] Qiaoyi Su, Yuhong Chou, Yifan Hu, Jianing Li, Shijie Mei, Ziyang Zhang, and Guoqi Li. Deep directly-trained spiking neural networks for object detection. In *Proceedings of the IEEE/CVF International Conference on Computer Vision (ICCV)*, pages 6532–6542, 2023.
- [44] Antti Tarvainen and Harri Valpola. Mean teachers are better role models: Weight-averaged consistency targets improve semi-supervised deep learning results. *Neural Information Processing Systems*, 2017.
- [45] Dmitrii Torbunov, Yihui Ren, Animesh Ghose, Odera Dim, and Yonggang Cui. EvRT-DETR: Latent Space Adaptation of Image Detectors for Event-based Vision. In *International Conference on Computer Vision (ICCV)*, 2025.
- [46] Carmen Martin Turrero, Maxence Bouvier, Manuel Breitenstein, Pietro Zanuttigh, and Vincent Parret. ALERT-transformer: Bridging asynchronous and synchronous machine learning for real-time event-based spatio-temporal data. In *Forty-first International Conference on Machine Learning*, 2024.
- [47] Shenqi Wang, Yingfu Xu, Amirreza Yousefzadeh, Sherif Eissa, Henk Corporaal, Federico Corradi, and Guangzhi Tang. Sparse convolutional recurrent learning for efficient event-based neuromorphic object detection. *arXiv preprint arXiv:2506.13440*, 2025.

- [48] Xiao Wang, Yu Jin, Wentao Wu, Wei Zhang, Lin Zhu, Bo Jiang, and Yonghong Tian. Object detection using event camera: A moe heat conduction based detector and a new benchmark dataset. In *Proceedings of the IEEE/CVF Conference on Computer Vision and Pattern Recognition (CVPR)*, 2025.
- [49] Ziyi Wu, Mathias Gehrig, Qing Lyu, Xudong Liu, and Igor Gilitschenski. LEOD: Label-Efficient Object Detection for Event Cameras. In *2024 IEEE/CVF Conference on Computer Vision and Pattern Recognition (CVPR)*, 2024. doi: 10.48550/arXiv.2311.17286.
- [50] Mengde Xu, Zheng Zhang, Han Hu, Jianfeng Wang, Lijuan Wang, Fangyun Wei, Xiang Bai, and Zicheng Liu. End-to-end semi-supervised object detection with soft teacher. *Proceedings of the IEEE/CVF International Conference on Computer Vision (ICCV)*, 2021.
- [51] Nan Yang, Yang Wang, Zhanwen Liu, Meng Li, Yisheng An, and Xiangmo Zhao. Smamba: Sparse mamba for event-based object detection. *Proceedings of the AAAI Conference on Artificial Intelligence*, 39(9):9229–9237, 2025. doi: 10.1609/aaai.v39i9.32999.
- [52] Alex Zihao Zhu, Liangzhe Yuan, Kenneth Chaney, and Kostas Daniilidis. Unsupervised Event-Based Learning of Optical Flow, Depth, and Egomotion. In *2019 IEEE/CVF Conference on Computer Vision and Pattern Recognition (CVPR)*, pages 989–997, 2019. doi: 10.1109/CVPR.2019.00108.
- [53] Nikola Zubić, Mathias Gehrig, and Davide Scaramuzza. State Space Models for Event Cameras. In *2024 IEEE/CVF Conference on Computer Vision and Pattern Recognition (CVPR)*, pages 5819–5828, 2024. doi: 10.1109/CVPR52733.2024.00556.

A Theoretical Justifications for Pillar Encoding

In this section, we provide the theoretical foundation for our Pillar Encoding (PE) formulation. To compress the continuous event signal, we project it onto an orthogonal polynomial basis using Legendre polynomials, $L_k(\tau)$, which satisfy the standard orthogonality and normalization condition $\langle L_k, L_m \rangle = \frac{2}{2k+1} \delta_{km}$ over the interval $[-1, 1]$ [1]. Building on this formulation, we establish two key guarantees of our architecture: (i) the truncated Legendre projection yields the unique minimizer of the L^2 functional reconstruction error over the polynomial subspace; and (ii) the density-aware numerical quadrature yields an unbiased temporal representation.

A.1 Optimality of the Truncated Orthogonal Projection

We model the temporal trajectory of the event features within a pillar as an underlying continuous, square-integrable function $h(\tau) \in \mathcal{H}$, where $\mathcal{H} = L^2([-1, 1])$ is a Hilbert space with the standard inner product $\langle f, g \rangle = \int_{-1}^1 f(\tau)g(\tau)d\tau$.

Proposition 1 (Optimality of Legendre Projection). *Let $h \in L^2([-1, 1])$, and let $\mathcal{S}_K = \text{span}\{L_0, L_1, \dots, L_{K-1}\}$, where $\{L_k\}_{k=0}^{K-1}$ are the Legendre polynomials, orthogonal with respect to the $L^2([-1, 1])$ inner product. Define*

$$h_K(\tau) = \sum_{k=0}^{K-1} a_k L_k(\tau), \quad \text{with} \quad a_k = \frac{2k+1}{2} \langle h, L_k \rangle.$$

Then h_K is the unique orthogonal projection of h onto \mathcal{S}_K , and hence $h_K = \arg \min_{g \in \mathcal{S}_K} \|h - g\|_{L^2}^2$.

Proof. Let $g(\tau) \in \mathcal{S}_K$ be an arbitrary polynomial in the subspace. We can analyze the squared L^2 error between the true signal h and the approximation g :

$$\|h - g\|^2 = \|(h - h_K) + (h_K - g)\|^2.$$

Expanding this expression using the properties of the inner product yields:

$$\|h - g\|^2 = \|h - h_K\|^2 + \|h_K - g\|^2 + 2\langle h - h_K, h_K - g \rangle.$$

To show that the cross-term vanishes, we must verify that the residual $(h - h_K)$ is orthogonal to every basis function L_m for $m \in \{0, \dots, K-1\}$. Evaluating the inner product:

$$\langle h - h_K, L_m \rangle = \langle h, L_m \rangle - \sum_{k=0}^{K-1} a_k \langle L_k, L_m \rangle.$$

By the orthogonality of the Legendre polynomials, $\langle L_k, L_m \rangle = \frac{2}{2m+1} \delta_{km}$, so the sum collapses to a single term:

$$\langle h - h_K, L_m \rangle = \langle h, L_m \rangle - a_m \left(\frac{2}{2m+1} \right).$$

Substituting the definition of $a_m = \frac{2m+1}{2} \langle h, L_m \rangle$, we obtain:

$$\langle h - h_K, L_m \rangle = \langle h, L_m \rangle - \langle h, L_m \rangle = 0.$$

Since $(h - h_K)$ is orthogonal to every basis vector in \mathcal{S}_K , and $(h_K - g)$ is a linear combination of these basis vectors, it follows that $\langle h - h_K, h_K - g \rangle = 0$. We are left with:

$$\|h - g\|^2 = \|h - h_K\|^2 + \|h_K - g\|^2.$$

Since $\|h - h_K\|^2$ is fixed for a given h and K , minimizing the total error requires minimizing $\|h_K - g\|^2$. By positive-definiteness of the norm, the minimum is achieved if and only if $\|h_K - g\|^2 = 0$, which implies $g = h_K$.

This proves that PE optimally projects the continuous feature trajectory into the K -dimensional polynomial coefficient space without relying on fixed temporal binning. \square

A.2 Unbiasedness of the Quadrature-Corrected Estimator

Event streams are asynchronous, meaning the temporal distribution of events is non-uniform. If an object accelerates, or if contrast changes, events arrive in dense bursts.

Proposition 2 (Bias of Naive Aggregation vs. Quadrature). *Let $\{\tau_n\}_{n=1}^N$ be an ordered sequence of timestamps with $\tau_1 < \dots < \tau_N$, sampled according to an inhomogeneous temporal density $\rho(\tau)$. Define $H_n := h(\tau_n)$, where $h : [-1, 1] \rightarrow \mathbb{R}$ is the underlying continuous-time signal. Let $\Delta\tau_n := \frac{1}{2}(\tau_{n+1} - \tau_{n-1})$ denote the local temporal spacing for interior points, with appropriate one-sided definitions at the boundaries.*

The naive empirical mean estimator \hat{I}_k^{naive} is biased by $\rho(\tau)$, whereas the quadrature estimator \hat{I}_k^{quad} asymptotically recovers the unscaled projection integral I_k .

Proof. The unscaled k -th Legendre projection integral is defined as:

$$I_k = \int_{-1}^1 h(\tau) L_k(\tau) d\tau.$$

The naive Monte Carlo estimator aggregates features uniformly across events:

$$\hat{I}_k^{\text{naive}} = \frac{2}{N} \sum_{n=1}^N H_n L_k(\tau_n).$$

As $N \rightarrow \infty$, by the Law of Large Numbers, this estimator converges to the expectation under $\rho(\tau)$:

$$\lim_{N \rightarrow \infty} \hat{I}_k^{\text{naive}} \propto \int_{-1}^1 h(\tau) L_k(\tau) \rho(\tau) d\tau \neq I_k.$$

Thus, \hat{I}_k^{naive} biases the representation toward regions with high event density ($\rho(\tau)$), distorting the true temporal trajectory $h(\tau)$.

Conversely, the trapezoidal quadrature estimator uses temporal weights $w_n \approx \Delta\tau_n$ [9, 36]:

$$\hat{I}_k^{\text{quad}} = \sum_{n=1}^N w_n H_n L_k(\tau_n).$$

This corresponds to a Riemann sum over a non-uniform partition. As the maximum spacing vanishes ($\max_n \Delta\tau_n \rightarrow 0$), the sum converges to the integral [38]:

$$\lim_{\max_n \Delta\tau_n \rightarrow 0} \sum_{n=1}^N w_n H_n L_k(\tau_n) = \int_{-1}^1 h(\tau) L_k(\tau) d\tau = I_k.$$

Therefore, the quadrature estimator yields an asymptotically unbiased estimate of the unscaled continuous-time projection integral.

In our final PE formulation (Section 3.1), the network computes the feature $z_{c,j,k} = \frac{1}{W_j} \hat{I}_k^{\text{quad}}$. The pillar-specific normalization term W_j converts the raw integral into a duration-normalized average. Rather than claiming strict L^2 -optimality at this final output stage, we note that this formulation ensures the model learns a density-invariant, duration-normalized temporal feature, stabilizing the inputs for subsequent network layers. \square

B Additional Quantitative Results

B.1 Detection Performance Preservation

Figure 2 shows the mAP of S5-ViT-B, EvRT-DETR-B, FATE-S, and FATE-E on Gen1, highlighting how well each method preserves performance as frequency increases from 20 Hz to 200 Hz. Both

FATE-E and FATE-S consistently outperform their respective backbones, with gains that grow at higher frequencies.

While FATE-E achieves stronger overall performance, the gap between FATE-E and FATE-S narrows as frequency increases. This trend reflects the advantage of state-space modeling in S5-ViT-B, which captures temporal dynamics more effectively under extreme sparsity.

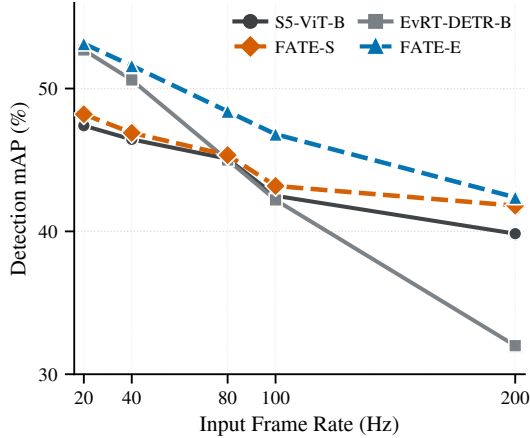


Figure 2: Comparison of mAP across different operating frequencies on Gen1.

B.2 Effect of Dense Temporal Supervision

We randomly sample 10,000 predicted bounding boxes from the Gen1 test set using two baseline detectors augmented with PE: PE + S5-ViT-B and PE + EvRT-DETR-B, both operating at 20 Hz. Figure 3 shows the precision–recall trade-off for the *car* and *pedestrian* classes. Pseudo-labels for cars consistently achieve higher precision and recall than those for pedestrians, likely due to the more consistent geometric structure of vehicles.

Decoupled Thresholds. To ensure high-quality supervision, we adopt decoupled thresholds: a lower tracking threshold of 0.3 to favor recall (reducing missed detections), and a higher detection threshold of 0.6 to promote precision (limiting false positives). As shown in Figure 3, these choices provide a consistent balance of high recall and precision, respectively.

Pseudo Label Quality. Table 5 provides a detailed evaluation of pseudo-label quality across frequencies from 20 Hz to 200 Hz, revealing three key insights for downstream supervision.

- *Temporal sparsity and performance decay:* All metrics—precision, recall, and localization accuracy (Median IoU)—degrade monotonically as frequency increases. At 200 Hz, the shortened accumulation window leads to sparse event representations, making it difficult to recover coherent object geometry. For example, the proportion of boxes with $\text{IoU} > 0.5$ for cars drops from 83.0% at 20 Hz to 65.2% at 200 Hz for PE + EvRT-DETR-B, highlighting a trade-off between temporal resolution and label reliability.
- *Architectural robustness:* Across all frequencies, PE + EvRT-DETR-B outperforms PE + S5-ViT-B, in line with the EvRT-DETR-B and S5-ViT-B comparisons in the main text. The DETR-based model maintains stronger spatial alignment, achieving a median $\text{IoU} \geq 0.5$ for cars even at 200 Hz, whereas the ViT-based baseline drops to 0.47, indicating greater robustness to noise and sparsity in high-frequency event data. Nevertheless, FATE-E and FATE-S, which adopt PE augmented by FAT, improve EvRT-DETR-B and S5-ViT-B, respectively, demonstrating consistent gains across heterogeneous architectures.
- *Class-wise variance (cars vs. pedestrians):* A consistent gap exists between object categories. Pseudo-labels for cars exhibit higher quality than those for pedestrians (e.g., 0.83 vs. 0.72 precision at 20 Hz), likely due to larger spatial extent and more rigid motion. In contrast, pedestrians suffer from fragmentation effects at high frequencies, with recall decreasing to 0.32–0.36 at 200 Hz.

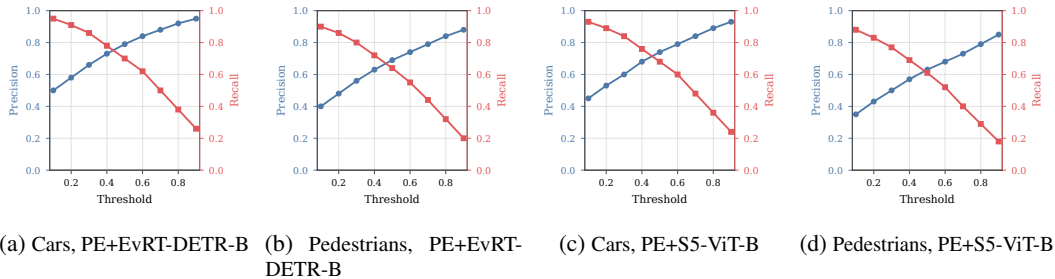


Figure 3: Precision and recall of pseudo-labels for cars and pedestrians on 10K samples randomly drawn from Gen1.

Table 5: Quality of generated pseudo labels on Gen1 for cars and pedestrians. We sample 10k boxes per frequency and evaluate against ground truth nearest in time.

Model	Freq.	Cars				Pedestrians			
		Precision \uparrow	Recall \uparrow	Med IoU \uparrow	IoU > 0.5 \uparrow	Precision \uparrow	Recall \uparrow	Med IoU \uparrow	IoU > 0.5 \uparrow
PE + S5-ViT-B	20 Hz	0.78	<u>0.64</u>	<u>0.62</u>	0.78	0.68	<u>0.52</u>	<u>0.54</u>	0.68
	40 Hz	0.75	0.60	0.59	0.74	0.65	0.48	0.51	0.64
	80 Hz	0.70	0.54	0.55	0.69	0.60	0.43	0.47	0.60
	100 Hz	0.66	0.50	0.52	0.66	0.57	0.40	0.44	0.56
	200 Hz	0.60	0.42	0.47	0.45	0.49	0.32	0.40	0.49
PE + EvRT-DETR-B	20 Hz	0.83	0.68	0.65	0.83	0.72	0.56	0.57	0.72
	40 Hz	<u>0.80</u>	<u>0.64</u>	<u>0.62</u>	<u>0.80</u>	<u>0.69</u>	<u>0.52</u>	<u>0.54</u>	<u>0.69</u>
	80 Hz	0.75	0.58	0.58	0.75	0.64	0.47	0.50	0.48
	100 Hz	0.72	0.54	0.55	0.72	0.61	0.44	0.47	0.44
	200 Hz	0.65	0.46	0.48	0.47	0.53	0.36	0.42	0.38

Training Strategy Ablations. Furthermore, we compare FAT to three ablated training strategies across frequencies:

- *Multi-frequency training (no additional supervision):* The detector is trained across multiple accumulation windows (20–200 Hz) using only sparse ground-truth annotations. For each frequency, the nearest labels are reused without introducing intermediate supervision, isolating the effect of multi-frequency exposure.
- *Consistency-only training (no densification):* A consistency loss is enforced between predictions at different frequencies, while supervision remains limited to sparse ground-truth annotations, without generating dense labels.
- *Naive annotation interpolation:* Dense supervision is introduced by linearly interpolating ground-truth bounding boxes across timestamps to generate high-frequency labels. These interpolated annotations are used for training at all frequencies, assuming smooth motion.

Table 6 shows that multi-frequency training improves high-frequency performance over the base detector (e.g., +4.08 mAP at 200 Hz for PE + EvRT-DETR-B) but leads to suboptimal accuracy at the canonical training frequency. Consistency-only training yields comparable results. Introducing dense supervision via naive interpolation improves mAP across all frequencies, motivating FAT, but its effectiveness is limited by noisy supervision (e.g., when adjacent frames do not share the same object instance). FAT achieves the best performance across all frequencies, indicating that integrating multi-frequency training, student-teacher consistency, and pseudo-label generations based on tracking-by-detection is key to robust detection across varying temporal resolutions in event-based settings.

Impact of temporal polynomial degree and pooling mechanisms. We conduct a comprehensive sensitivity analysis of the temporal polynomial degree (K) and pooling strategies on the Gen1 benchmark.

In Table 7, performance improves as K increases from 2 to 3, but degrades for $K = 4$ and 5 despite the added complexity. Accordingly, we set $K = 3$, which achieves the best trade-off between

Table 6: FAT vs. ablated strategies in FATE-E on Gen1.

Method	Ground Truth	Dense Sup.	Pseudo-labels	mAP (%) \uparrow				
				20Hz	40Hz	80Hz	100Hz	200Hz
PE + EvRT-DETR-B	✓	✗	✗	51.94	50.31	46.06	44.10	36.40
Multi-frequency	✓	✗	✗	49.24	47.06	45.70	43.12	40.48
Consistency-only	✓	✗	✓	48.90	47.85	45.40	43.80	41.10
Naive interpolation	✓	✓	✗	51.18	49.37	47.21	45.41	41.64
FAT (ours)	✓	✓	✓	53.14	51.60	48.40	46.80	42.38

performance and complexity. Moreover, we adopt a temporal basis with trapezoidal weighting, which consistently outperforms the baseline strategies.

Since these hyperparameters primarily control temporal feature compression rather than spatial resolution, the optimal configuration identified in Table 7 ($K = 3$ with trapezoidal weighting) generalizes effectively to higher-resolution settings, as reflected in the 1Mpx results reported in the main text.

Table 7: Sensitivity of temporal polynomial degree K and temporal pooling methods in PE across operating frequencies on Gen1 test set.

Variant	20 Hz			100 Hz			200 Hz		
	mAP	AP ₅₀	AP ₇₅	mAP	AP ₅₀	AP ₇₅	mAP	AP ₅₀	AP ₇₅
$K = 2$	46.32	76.00	49.80	38.20	65.50	40.30	29.90	54.80	30.20
$K = 3$	51.94	81.20	55.10	44.10	71.90	46.20	36.40	61.80	36.80
$K = 4$	50.71	79.95	53.90	42.82	70.40	44.80	34.88	59.90	35.10
$K = 5$	49.80	78.90	52.70	43.50	70.50	44.22	33.60	58.20	33.80
Max Pooling	46.10	72.80	50.50	38.90	66.10	42.00	29.40	54.20	29.80
Temporal Basis + Uniform Weights	51.63	80.90	54.80	43.70	71.20	45.60	35.60	60.50	35.70
Temporal Basis + Trapezoidal Weights	51.94	81.20	55.10	44.10	71.90	46.20	36.40	61.80	36.80

Impact of the pillar size. We perform a spatial pillar size ablation at an intermediate operating frequency of 100 Hz. Since spatial quantization primarily affects the morphological resolution of targets rather than their temporal dynamics, the optimal spatial scale remains largely invariant to the choice of temporal frequency.

Table 8 highlights a key architectural trade-off between spatial resolution and global context preservation. As the pillar size decreases from 8 to 2, performance improves steadily, reaching a peak mAP of 46.80%, indicating that finer spatial discretization more effectively captures the fine-grained structure of moving targets.

However, further reducing the pillar size to 1 leads to a performance drop. This inflection arises from the fixed resolution budget of $P = 16,000$ pillars per sample; at a pillar size of 1, the grid expands to 81,920 possible pillars, requiring the model to discard over 80% of spatial locations. In practice, a pillar size of 2 provides the best trade-off—preserving spatial fidelity while avoiding severe information loss due to pillar truncation.

On Gen1, event statistics show that $N = 32$ (samples per pillar) is sufficient for over 99% of active pillars (using a spatial size of 2×2). Only a small $\sim 1\%$ tail exceeds this threshold, primarily during longer 50 ms accumulation windows. At higher temporal resolutions (5–10 ms), event counts fall well below 32. Thus, setting $N = 32$ safely captures local temporal dynamics while avoiding excessive memory waste in sparse pillars.

B.3 Sensitivity Ablations of Pillar Encoding

Impact of Temporal Channel Dimension. Table 9 presents the effect of the temporal channel dimension, C , on detection performance across different operating frequencies. Empirically, we observe a consistent performance peak at $C = 64$, which yields the highest mAP at 20 Hz, 100 Hz, and 200 Hz among the evaluated configurations. Increasing the capacity from $C = 32$ to $C = 64$ leads to steady gains, suggesting that sufficient channel width is necessary to capture complex temporal dynamics effectively.

Table 8: Sensitivity of pillar size choices in PE on the Gen1 test set at 100 Hz.
x Fixed: $P = 16,000$, $C = 64$, $K = 3$, $N = 32$

Pillar size	Grid ($H \times W$)	Total pillars	Max pillars P	mAP (%) \uparrow	AP ₅₀ (%) \uparrow	AP ₇₅ (%) \uparrow
8	32×40	1,280	1,280	43.18	69.20	45.10
4	64×80	5,120	5,120	45.73	72.60	47.80
2	128×160	20,480	16,000	46.80	73.10	49.10
1	256×320	81,920	16,000	46.09	71.90	48.20

Table 9: Impact of temporal capacity C on the Gen1 test set.

Fixed: Pillar size = 2, $P = 16,000$, $K = 3$, $N = 32$

Channel dimension C	20 Hz			100 Hz			200 Hz			#Params (M)
	mAP	AP ₅₀	AP ₇₅	mAP	AP ₅₀	AP ₇₅	mAP	AP ₅₀	AP ₇₅	
$C = 32$	52.48	81.70	56.10	45.71	71.90	47.70	40.64	65.90	40.80	57.151
$C = 48$	52.86	82.00	56.50	46.22	72.50	48.20	41.72	67.10	41.70	57.156
$C = 64$	53.14	82.30	56.80	46.80	73.10	49.10	42.38	68.20	42.50	57.161
$C = 80$	53.08	82.20	56.70	46.69	72.90	48.70	42.21	67.90	42.20	57.166
$C = 96$	52.97	82.00	56.40	46.41	72.60	48.30	41.95	67.40	41.90	57.171

However, further scaling to $C = 80$ and $C = 96$ results in continuous performance degradation. Given the sparse and noisy nature of event data, excessive temporal capacity may encourage overfitting to localized sensor noise rather than promoting robust, generalizable motion representations. Notably, the configuration at $C = 64$ achieves best performance within our tested range while introducing only 0.01M additional parameters compared to the $C = 32$ baseline, indicating a favorable trade-off between temporal expressiveness and model efficiency.

Efficiency Ablation Table 10 highlights the efficiency of our proposed approach. Integrating PE into the EvRT-DETR-B baseline effectively compresses the continuous event stream while introducing a negligible latency overhead of only 0.1 ms, which is 0.87–1.16% of the inference latency.

However, applying PE alone leads to a slight performance drop, suggesting that standard backbones are not well-suited to fully exploit the resulting dense representation without dedicated temporal modeling. Incorporating the offline FAT module resolves this limitation, boosting performance to a peak mAP of 53.14. Notably, this gain is achieved without any additional parameters or inference latency compared to the PE-only variant.

Overall, FATE-E and FATE-S consistently outperforms the strong EvRT-DETR-B and S5-ViT-B baselines, respectively, with minimal overhead of additional parameters and 0.1 ms ($\sim 1\%$) end-to-end inference latency increase on an NVIDIA T4 GPU.

C Qualitative Results

Figure 4 presents a qualitative comparison of bounding boxes at 20 Hz. The strongest baselines exhibit missed detections and temporal instability, whereas FATE-E, equipped with our PE at inference, produces stable predictions, particularly for small or weakly activated targets.

Figures 5 and 6 further highlight the impact of our FAT. The ablation shows that FATE-E trained with bounding box tracking achieves superior performance over the variant without detection-by-tracking supervision.

D Reproduction Details

This section provides implementation details, hyperparameter settings, and dataset preprocessing procedures that were omitted from the main text for brevity. An anonymized ZIP archive is included with the submission, and the code along with the high-frequency event-based datasets will be released publicly upon acceptance.

Table 10: Efficiency ablations of FATE-E and FATE-S on the Gen1 test set at 20, 100, and 200 Hz.

Model	Params (M)↓	20 Hz		100 Hz		200 Hz	
		mAP↑	Latency (ms)↓	mAP↑	Latency (ms)↓	mAP↑	Latency (ms)↓
EvRT-DETR-B	57.14	52.70	11.4	42.20	11.4	32.00	11.4
+ PE	57.16	51.94	11.5	44.10	11.5	36.40	11.5
+ PE + FATE (FATE-E)	57.16	53.14	11.5	46.80	11.5	42.38	11.5
S5-ViT-B	18.19	47.40	8.5	42.49	8.5	39.84	8.5
+ PE	18.33	47.70	8.6	43.08	8.6	39.30	8.6
+ PE + FATE (FATE-S)	18.33	48.20	8.6	43.18	8.6	40.80	8.6

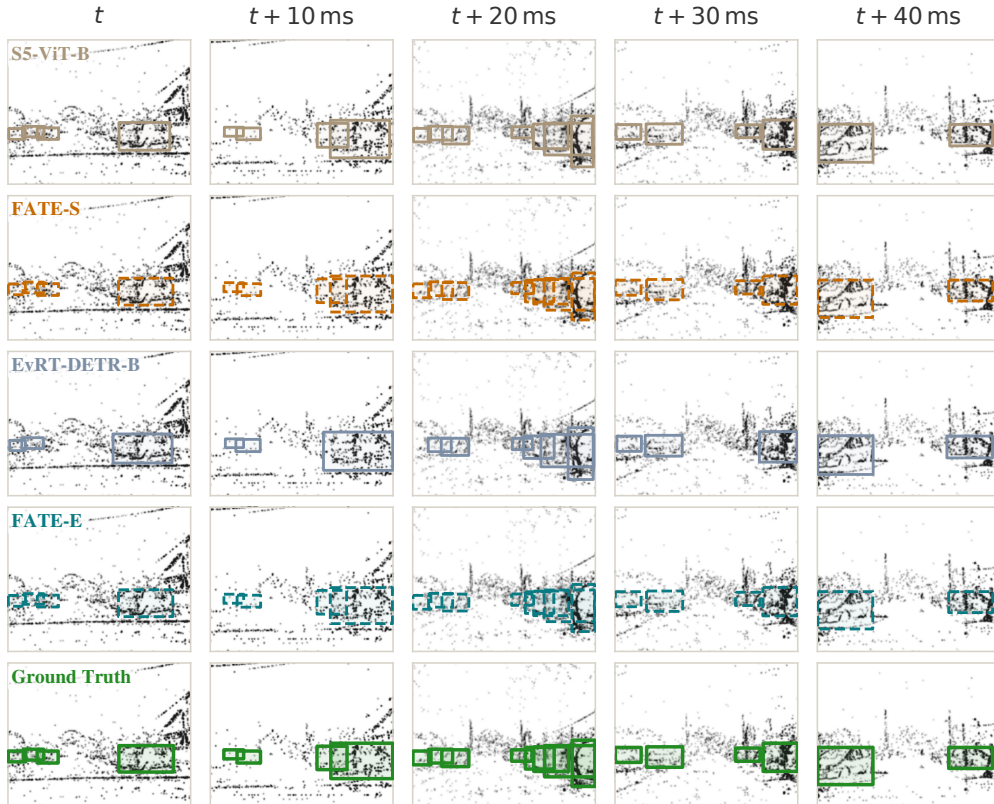


Figure 4: Qualitative comparison of bounding boxes (Gen1, 20 Hz).

D.1 Datasets and Preprocessing

We evaluate our method and the baselines on two standard event-based object detection benchmarks, Gen1 [10] and 1Mpx [35], which differ substantially in resolution and annotation density. In particular, Gen1 provides sparse annotations (1–4 Hz), requiring stronger temporal aggregation or densification strategies, whereas 1Mpx offers high frame-rate, dense annotations (~ 60 Hz), enabling finer-grained temporal supervision.

To ensure consistency with prior work and the official EvRT-DETR [45] and S5-ViT-B [53] implementations, we preserve the original input resolution settings after preprocessing. Specifically, Gen1 samples are padded to 256×320 , while 1Mpx samples are resized to 360×640 and subsequently padded to 384×640 .

To assess robustness across different temporal resolutions, we vary the event accumulation window to simulate multiple sensing frequencies, including 50 ms (20 Hz), 25 ms (40 Hz), 12.5 ms (80 Hz), 10 ms (100 Hz), and 5 ms (200 Hz). Higher temporal frequencies correspond to shorter accumulation windows, resulting in sparser event representations and reduced temporal context per input sample.

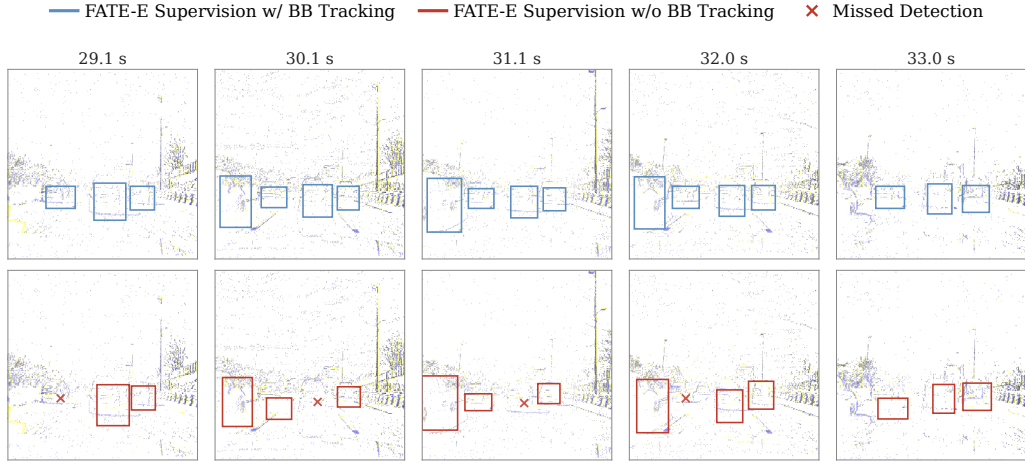


Figure 5: Visualization of the dense label supervision in FATE-E (Gen1, 20 Hz)

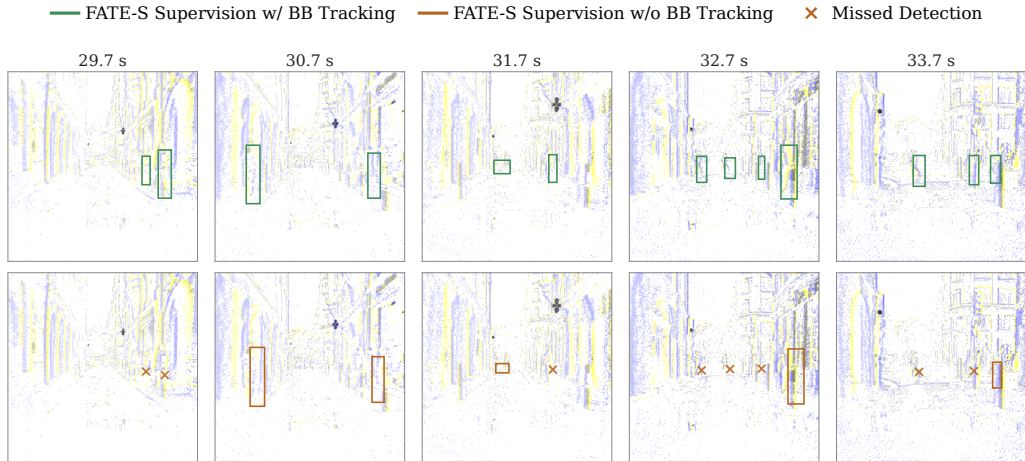


Figure 6: Visualization of the dense label supervision in FATE-S (Gen1, 20 Hz)

D.2 Pillar Encoding Configuration

We tune the architectural hyperparameters for Pillar Encoding—specifically the latent channel dimension C , the Legendre basis size K , and the spatial pillar size—through sensitivity ablations on the Gen1 dataset. For pillar size 2, we use $D = 7$ discarding the center offsets of events. Based on the results detailed in Tables 7, 8, and 9 (Appendix B), we adopt $C = 64$, $K = 3$, and a pillar size of 2 for both FATE-E and FATE-S, as this configuration consistently achieves the strongest detection performance across all evaluated operating frequencies.

D.3 Data Augmentation

To improve the performance and generalization of the proposed model while mitigating overfitting, we employ a comprehensive set of data augmentation techniques. These transformations encourage

the model to learn features that are robust to variations in orientation, scale, and partial occlusion. The augmentation pipeline used during training is as follows:

- *Random Horizontal Flip*: Applied with probability 0.5 to account for mirror symmetry in natural scenes.
- *Random Rotation*: Input event streams are rotated by an angle $\theta \in [-30^\circ, 30^\circ]$, improving robustness to non-upright sensor orientations.
- *Random Affine Translation*: Spatial shifts of up to 0.5 (relative to image dimensions) are applied along both x and y axes to increase robustness to object displacement and centering variability.
- *Scale Jitter*: Inputs are randomly scaled by a factor $s \in [0.5, 1.5]$, simulating variations in object distance and promoting multi-scale feature learning.
- *Shear*: A shearing transformation up to 30° is applied to model perspective distortions and oblique viewpoints.
- *Center Crop*: Used to maintain consistent input dimensions while preserving central spatial structure.
- *Random Erasing*: Applied with probability 0.4, where a randomly selected rectangular region is replaced with noise or zero values, simulating occlusions and encouraging reliance on partial and local features.

D.4 Multi-Frequency Pseudo-Label Generation

To densify supervision during Phase 1 of our Frequency-Aware Training, we apply the event detector (augmented by PE) sequentially over the full training split using the canonical event window of 50 ms. Recurrent states are preserved across clips of 21 frames for Gen1 and 10 frames for 1Mpx to maintain temporal continuity. Ground-truth bounding boxes are retained strictly at annotated timestamps, while pseudo-labels are generated only for unlabeled timestamps corresponding to the target temporal frequencies.

To ensure high-quality pseudo-supervision, raw detections are first filtered prior to temporal association. We apply an initial IoU threshold of 0.3 for tacking, followed by class-specific detection confidence thresholds of 0.6 for cars and 0.3 for pedestrians, applied to both objectness and classification scores. Subsequently, standard dataset-specific bounding box filtering is performed.

Finally, a tracking-by-detection post-processing step is used to enforce temporal consistency. To suppress short, noisy, or spurious trajectories produced by the event detector, we impose a minimum tracklet length L_{\min} . To account for increasing temporal resolution at higher sampling frequencies, this constraint is scaled proportionally, with $L_{\min} = 6$ at 20 Hz, $L_{\min} = 12$ at 40 Hz, and further increased accordingly for 80 Hz, 100 Hz, and 200 Hz.

D.5 Linear Curriculum Schedule

We employ a curriculum over the frequency-specific datasets. At training round r , the student frequency is sampled according to $f \sim p_r(f)$, which gradually shifts probability mass toward higher, sparser frequencies.

To ensure stable training from dense to sparse regimes, we adopt a linear schedule over the sampling distribution. Let $\mathcal{F} = \{f_{\min}, \dots, f_{\max}\}$ denote the ordered set of frequencies (e.g., 20, 40, 80, 100, 200 Hz), and let $r \in [0, R]$ denote the current training epoch. We define the normalized progress $\alpha_r = r/R \in [0, 1]$ to bias sampling toward higher frequencies as r increases.

The sampling distribution is given by:

$$p_r(f_i) = \frac{(1 - \alpha_r) \mathbf{1}_{f_i=f_{\min}} + \alpha_r w_i}{Z_r},$$

where $w_i = \frac{i}{|\mathcal{F}|}$ and Z_r is a normalization constant ensuring $\sum_{f_i \in \mathcal{F}} p_r(f_i) = 1$.

This schedule starts with sampling concentrated at the canonical frequency f_{\min} and gradually shifts toward higher frequencies as α_r increases. Frequencies are sampled independently per training sample

within a mini-batch, while the teacher network consistently operates at the canonical frequency f_c . We use this fixed linear curriculum for all experiments without additional hyperparameter tuning.

D.6 Tuning Hyperparameters

Models are trained using the AdamW optimizer with a weight decay of 1×10^{-4} and gradient clipping with a maximum norm of 5.0.

For the Gen1 variants, models are trained for 400 epochs with a batch size of 32. The temporal detectors are optimized using a OneCycle learning rate schedule [42] with a peak learning rate of 2×10^{-4} and a warm-up proportion of 0.005. Concurrently, the teacher network is updated via an exponential moving average (EMA) using a momentum decay of $\gamma = 0.9999$. For the 1Mpx variants, we maintain identical optimizer and scheduler configurations. Across all experimental settings, the transformer head utilizes 300 object queries and 100 denoising queries to facilitate robust bipartite matching and bounding box regression.

The event-wise MLP in Section 3.1 is trained jointly with the detector in an end-to-end manner. Specifically, each D -dimensional augmented event vector is projected via a shared linear layer followed by BatchNorm and ReLU into a C -dimensional latent embedding, and all MLP parameters are optimized together with the backbone and detection head using the same training configuration as the base detector. In the temporal encoding stage, the coefficients $\alpha_{c,k}$ and β_c (Eq. 7) are not manually tuned hyperparameters; instead, they are learned end-to-end as trainable parameters that linearly combine the K quadrature-corrected temporal moments within each channel.

We set the box regression weights of λ_{ℓ_1} to 5 and λ_{iou} to 2 (Eq. 9), commonly used for the bounding-box and GIoU terms. For the S5-ViT-B variant, we retain the YOLOX detection objective, where the box term is an IoU regression loss weighted by 5, together with objectness and classification losses. These values are standard for each category of detectors and needed no hyperparameter tuning.

All experiments are conducted on two NVIDIA A40 GPUs (48 GB GDDR6 each) for training and an NVIDIA T4 GPU (16 GB GDDR6) for evaluation. Training requires approximately two weeks per run, while evaluation takes about one week per method–dataset pair.

E Limitations

FATE is developed as a continuous-time encoding framework that integrates with standard synchronous detection backbones. Consequently, it operates on discrete accumulation windows $[t_1, t_2]$ to bridge asynchronous event streams and frame-based architectures. While the proposed time-normalized polynomial basis and FAT curriculum empirically yield strong robustness across a wide range of window durations and operating frequencies, eliminating the windowing mechanism entirely would require adopting fundamentally different downstream architectures (e.g., spiking neural networks or continuous-time state-space models). Such directions are orthogonal to our goal and are not necessary to validate the core contribution of this work, which is to improve temporal representations within existing detection pipelines.

Our formulation further adopts a fixed Legendre polynomial basis with trapezoidal quadrature. This design prioritizes simplicity, efficiency, and stability: low-order polynomials (e.g., $K = 3$) provide a compact representation of transient, non-periodic event dynamics, while trapezoidal integration offers a robust approximation for irregular, bursty event streams. Although more expressive alternatives—such as learned implicit representations, adaptive basis functions, or spline-based encodings—could increase representational flexibility, they also introduce additional complexity and confounding factors.

In this work, we intentionally restrict the design space to isolate the effect of a lightweight, structured temporal encoding. Within this scope, FATE demonstrates strong empirical performance and efficiency across frequencies and resolutions. Exploring more adaptive or fully continuous-time formulations represents a promising direction for future work, but lies beyond the targeted scope of this paper.

F Broader Impacts

The advancement of low-latency, event-based perception through the FATE framework has important implications for safety-critical systems. By improving robustness at high operating frequencies (e.g., 200 Hz), FATE can benefit applications that depend on fine-grained temporal resolution, including autonomous driving, aerial robotics, and mobile manipulation. In these settings, accurate high-frequency perception is critical for reliably capturing fast motion and reducing failure cases associated with motion blur or delayed reaction times. Furthermore, event-based vision possesses inherent privacy-preserving attributes; by recording only asynchronous brightness changes (e.g., structural edges and motion) rather than full-texture RGB frames, these sensors naturally obfuscate highly identifiable personal features compared to traditional cameras. In this sense, FATE effectively supports the stable and privacy-conscious deployment of event-based perception in real-world dynamic environments.

At the same time, these capabilities may also introduce dual-use considerations. The enhanced ability to reliably detect and track objects at extremely high frequencies and under challenging illumination conditions could be applied in domains such as pervasive surveillance or military sensing systems, where automated tracking and decision-making raise ethical concerns.

FATE is a general-purpose perception module that operates purely at the representation and detection level, without incorporating application-specific decision-making or control logic. As such, it does not in itself require task- or domain-specific safeguards. Its real-world impact is instead determined by the downstream systems in which it is integrated, where appropriate safety measures, governance, and regulatory oversight should be applied. We encourage continued discussion within the community on the responsible deployment of high-frequency perception systems.

G Public Resources Used

In this section, we acknowledge the public resources used during the course of this work.

G.1 Public Datasets Used

- **Gen1** Prophesee Gen1 Automotive Detection Dataset License
- **1 Mpx** Prophesee 1Mpx Automotive Detection Dataset License

G.2 Public Implementations Used

- **RVT** MIT License
- **SSM** Apache-2.0 license
- **LEOD** MIT License
- **EvRT-DETR** BSD-3 License